

Spectroscopic follow-up of black hole and neutron star candidates in ellipsoidal variables from *Gaia* DR3

Pranav Nagarajan,¹★ Kareem El-Badry,^{1,2} Antonio C. Rodriguez,¹ Jan van Roestel,^{3,1} and Benjamin Roulston¹

¹*Department of Astronomy, California Institute of Technology, 1200 E. California Blvd., Pasadena, CA 91125, USA*

²*Center for Astrophysics | Harvard & Smithsonian, 60 Garden Street, Cambridge, MA 02138, USA*

³*Anton Pannekoek Institute for Astronomy, University of Amsterdam, 1090 GE Amsterdam, The Netherlands*

Accepted 2023 July 9. Received 2023 June 23; in original form 2023 April 12

ABSTRACT

We present multi-epoch spectroscopic follow-up of a sample of ellipsoidal variables selected from *Gaia* DR3 as candidates for hosting quiescent black holes (BHs) and neutron stars (NSs). Our targets were identified as BH/NS candidates because their optical light curves – when interpreted with models that attribute variability to tidal distortion of a star by a companion that contributes negligible light – suggest that the companions are compact objects. From the likely BH/NS candidates identified in recent work accompanying *Gaia* DR3, we select 14 of the most promising targets for follow-up. We obtained spectra for each object at 2–10 epochs, strategically observing near conjunction to best-constrain the radial velocity semi-amplitude. From the measured semi-amplitudes of the radial velocity curves, we derive minimum companion masses of $M_{2,\min} \leq 0.5 M_{\odot}$ in all cases. Assuming random inclinations, the typical inferred companion mass is $M_2 \sim 0.15 M_{\odot}$. This makes it unlikely that any of these systems contain a BH or NS, and we consider alternative explanations for the observed variability. We can best reproduce the observed light curves and radial velocities with models for unequal-mass contact binaries with starspots. Some of the objects in our sample may also be detached main-sequence binaries, or even single stars with pulsations or starspot variability masquerading as ellipsoidal variation. We provide recommendations for future spectroscopic efforts to further characterize this sample and more generally to search for compact object companions in close binaries.

Key words: Compact Objects (288) — Ellipsoidal Variable Stars (455)

1 INTRODUCTION

The Milky Way is thought to contain $\sim 10^8$ stellar-mass black holes (BHs) and $\sim 10^9$ neutron stars (NSs), an uncertain fraction of which are in binaries (Brown & Bethe 1994; Chawla et al. 2022). Many theoretical models predict that binaries containing non-accreting BHs and NSs should significantly outnumber accreting systems, which are likely a rare outcome of binary evolution (e.g. Portegies Zwart et al. 1997). However, almost all known stellar-mass BHs are accreting from a companion and were discovered via their emission at X-ray and/or radio wavelengths. Similarly, all unambiguously identified neutron stars are either in accreting binaries or are radio pulsars. There are several ongoing attempts to find dormant BHs and NSs in wider binaries, but it has become clear in recent years that these systems are relatively rare and false-positives are abundant (e.g. El-Badry & Quataert 2021; El-Badry & Burdge 2022; El-Badry et al. 2022a; El-Badry et al. 2022b). To date, only ~ 20 BHs have been dynamically confirmed (McClintock & Remillard 2006; Corral-Santana et al. 2016).

The recent 3rd data release of the *Gaia* mission (“*Gaia* DR3”; Prusti et al. 2016; Vallenari et al. 2022) is a treasure trove for studies of binary evolution and searches for rare objects. *Gaia* produces

catalogs of astrometric, spectroscopic, and photometrically variable binaries (Eyer et al. 2022; Mowlavi et al. 2022; Halbwachs et al. 2022; *Gaia* Collaboration et al. 2022). Several recent studies have searched for NS/BH companions in the astrometric and spectroscopic binary samples published in DR3 (e.g. Shahaf et al. 2023; El-Badry et al. 2022d; El-Badry et al. 2023; Chakrabarti et al. 2023; El-Badry & Rix 2022; Fu et al. 2022). In this study, we focus on the sample of ellipsoidal variable binaries detected via *Gaia* light curves. Ellipsoidal variability is sensitive to BH/NS companions in *close* binaries; i.e., the immediate progenitors of X-ray binaries.

Recently, Gommel et al. (2021a) introduced a new method to identify ellipsoidal variables hosting massive, unseen companions based on their light curves alone. Subsequently, Gommel et al. (2022) applied the method to the sample of candidate ellipsoidal variables published in DR3. They identified 262 sources whose light curves suggested the presence of an unseen companion more massive than the luminous primary, potentially indicative of a compact object. There has thus far been no spectroscopic follow-up of this sample of candidate BH/NS companions. While comparably large samples of ellipsoidal variables have been produced previously from photometric surveys before *Gaia* (e.g. with OGLE; see Gommel et al. 2021b), the *Gaia* DR3 sample is all-sky and dominated by relatively bright stars amenable for spectroscopic follow-up.

Since compact object binaries are an intrinsically rare popula-

★ E-mail: pnagaraj@caltech.edu

tion, vetting through spectroscopic follow-up is essential. This paper presents a spectroscopic pilot study of the [Gomel et al. \(2022\)](#) *Gaia* DR3 sample, with a goal of measuring dynamical masses and searching for luminous companions in a subset of their most promising candidates. This allows us to assess the purity of the full sample and diagnose the most common false-positives.

The remainder of this paper is organized as follows. In Section 2, we summarize the origin of ellipsoidal variability and the search strategy for high mass ratio companions proposed by [Gomel et al. \(2021a\)](#). In Section 3, we discuss how we selected the most promising variables for spectroscopic follow-up and describe the follow-up observations. In Section 4, we analyze the radial velocities and infer companion masses. Finally, in Section 5, we discuss possible failure modes of the selection strategy used by [Gomel et al. \(2022\)](#) including contact binaries, binaries containing spotted stars, and single stars with pulsational or starspot variability mistaken for tidal deformation. We summarize our results in Section 6.

2 A MINIMUM MASS RATIO INFERRED FROM ELLIPSOIDAL VARIABILITY

In a close binary, tidal forces can distort one or both stars into a teardrop shape. The resulting time-variable geometric cross-section leads to photometric variability with a period of half the orbital period. The amplitude of this “ellipsoidal” variability depends on the orbital inclination, the mass ratio $q = M_2/M_1$, where M_1 is the star dominating the optical light, and the Roche lobe filling factor of the distorted luminous primary (M_1 ; e.g. [Morris & Naftilan 1993](#)). In general, the variability amplitude is largest for edge-on inclinations and is largest in binaries with large mass ratios and Roche lobe filling factors approaching unity.

While the inclination and Roche lobe filling factor are generally unknown, they cannot be larger than 90 degrees and unity, respectively. Recently, [Gomel et al. \(2021a\)](#) demonstrated that, under the assumption that all variability is indeed due to tidal deformation, this fact can be used to infer a stringent lower limit on the mass ratio of an ellipsoidal variable. This quantity, which they term the “modified minimum mass ratio” (mMMR or \hat{q}_{\min}), is robust to assumptions about the mass, radius, and evolutionary state of the component stars ([Gomel et al. 2020, 2021a](#)). In brief, Gomel et al. show that under the assumptions of their model, a variability half-amplitude larger than ≥ 0.1 mag can only occur if the mass ratio is larger than one; i.e., if the unseen companion is more massive than the source itself. This reflects the fact that a Roche-lobe filling star is more tidally distorted when the mass ratio is large than when it is small. The expected variability amplitude in a given photometric band can be calculated straightforwardly for a given mass ratio, inclination, and Roche lobe filling factor using tabulated approximations (e.g. [Morris & Naftilan 1993](#); [Gomel et al. 2020](#)).

[Gomel et al. \(2022\)](#) analyzed the *Gaia* DR3 photometrically-variable binaries using this strategy to identify binaries with large \hat{q}_{\min} . Starting with ~ 20 million possible ellipsoidal systems, and only including systems with well-constrained periods < 2.5 days, reliable and significant variability amplitudes, and $\hat{q}_{\min} > 0.5$, they identified 262 high-confidence ellipsoidal variables near the main-sequence whose variability amplitudes imply mass ratios larger than unity at the one-sigma level. Their sample is restricted to sources near the main-sequence in the color-magnitude diagram, with the goal of excluding mass-transfer binaries in which $q > 1$, but the companion is a main-sequence star (“Algol-type” binaries; e.g. [Clavel et al. 2021](#); [El-Badry et al. 2022b](#)).

3 DATA

3.1 Sample Selection

From the 6306 probable ellipsoidal variables identified by [Gomel et al. \(2022\)](#), we selected 14 bright candidates with high minimum mass ratios for spectroscopic follow-up. We limited the sample to variables with apparent *G*-band magnitude < 17 and well-constrained distances ($\text{parallax_over_error} > 3$). We further restricted the sample to targets with declination $\delta > -30^\circ$, which were observed by the Pan-STARRS survey ([Chambers et al. 2016](#)) and thus have well-constrained extinctions from the 3D dust map of [Green et al. \(2019\)](#). Then, we investigated the variables with $\hat{q}_{\min} \geq 0.8$ by hand, verifying that their optical light curves from Public Data Release 12 of the Zwicky Transient Facility (ZTF; [Bellm et al. 2019](#)) (queried from IRSA using `ztquery`; see [Rigault 2018](#)) indeed appear to be dominated by ellipsoidal variability.

It was immediately clear that a significant fraction of the candidates fall above the main sequence in the extinction-corrected color-magnitude diagram (Figure 1), as is expected for binaries containing two luminous stars that both contribute significantly to the total flux. Such binaries are unlikely to host massive dark companions, so we prioritized sources that are not significantly above the main sequence in our spectroscopic follow-up.

The series of cuts leading to our final sample of 14 probable ellipsoidal variables with spectroscopic observations is displayed on the de-reddened *Gaia* CMD in Figure 1, with the blue points in the background of each CMD representing a random comparison sample of ~ 45000 stars for *Gaia* DR3 with declination $\delta > -30^\circ$ and apparent *Gaia G*-band magnitude $G < 17$. The initial cut (which restricted the sample to bright variables with $G < 17$) was most important, as it reduced the size of the initial sample of variables with available extinctions by more than a factor of 6. While most of the candidates in this sample also had well-constrained distances (i.e. a relative parallax / error > 3) and well-sampled ZTF light curves (i.e. ≥ 20 epochs in the ZTF *g*-band), we found that a majority of the sample still lied above the main sequence. Hence, from this vetted sample, we chose a set of 12 promising variables near the main sequence of the comparison sample that had been identified by [Gomel et al. \(2022\)](#) to have inferred $\hat{q}_{\min} > 0.8$. For the sake of completeness, and to investigate the effect of selection bias, we also observed two candidates with $0.5 < \hat{q}_{\min} < 0.8$. Our final sample of 14 candidate ellipsoidal variables has apparent *G*-band magnitudes between 16 and 17 and orbital periods ranging from about 0.27 days to about 0.75 days. They are located on the upper main sequence on the CMD (i.e. bluer than $G_{BP} - G_{RP} = 1$) and have likely primary masses between $1 - 2 M_\odot$ (see Section 4.3 for details). Their light curve-inferred minimum mass ratios are typically ≈ 1.0 , as might be expected for NS or low-mass BH companions.

As an example, we provide ZTF *g*-band, ZTF *r*-band, and *Gaia G*-band light curves for a typical ellipsoidal variable candidate and an anomalous ellipsoidal variable candidate in Figure 2. For the typical ellipsoidal variable candidate, the characteristic periodicity and difference in light curve minima is evident; for this variable, the peak-to-peak variability amplitude is 0.135, and the corresponding modified minimum mass ratio (mMMR or \hat{q}_{\min}) inferred by [Gomel et al. \(2022\)](#) is 1.01 ± 0.26 . On the other hand, the anomalous ellipsoidal variable candidate displays an uncharacteristic difference in light curve maxima, and was thus not considered in our final sample. In both cases, it is clear that using ZTF photometry often represents an improvement over the relatively sparsely sampled *Gaia* light curves. On the other hand, the photometric precision of the *Gaia* light curves is generally higher than that of the ZTF data.

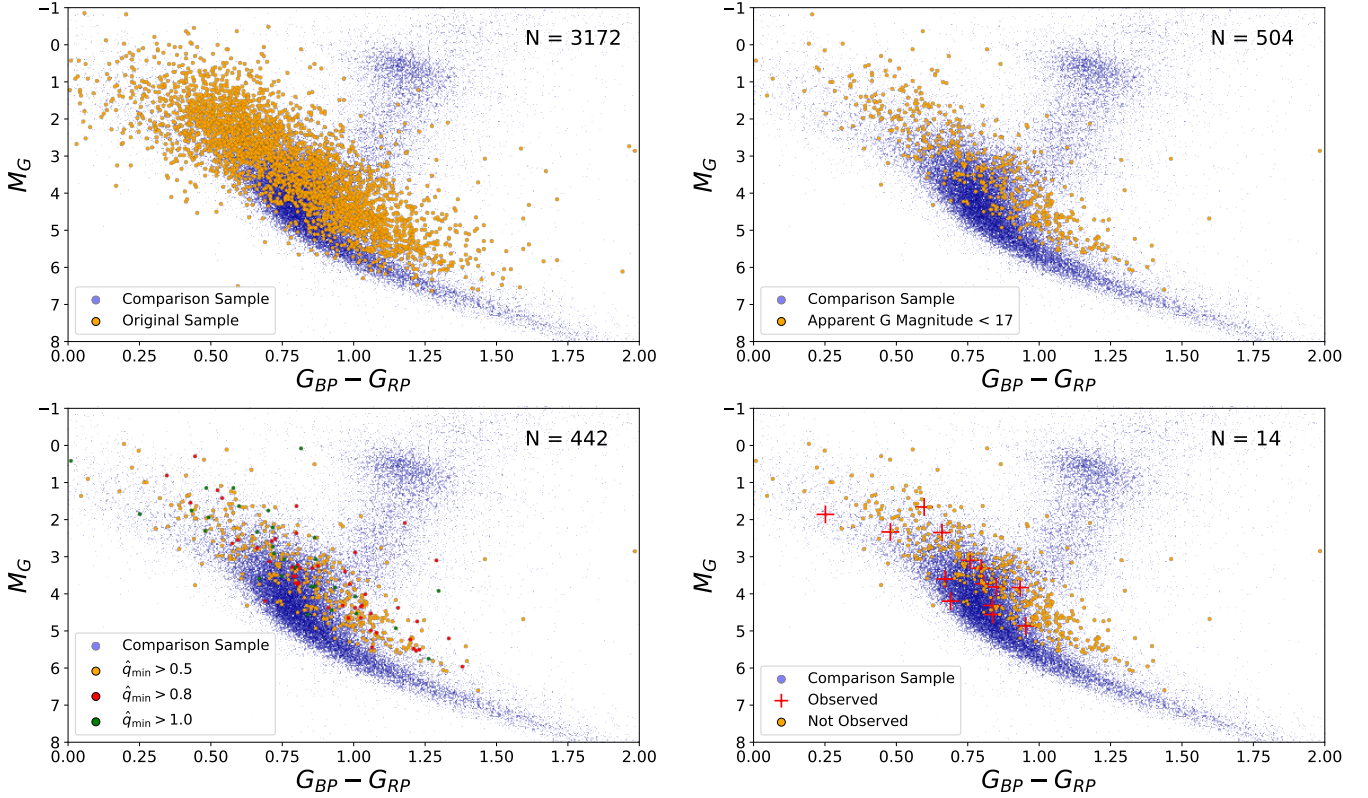


Figure 1. Color-magnitude diagrams visualizing our sample selection. The upper left panel displays the original sample of ellipsoidal variables (i.e. objects in the [Gomel et al. \(2022\)](#) catalog that have available extinctions) plotted over a random comparison sample of ~ 45000 stars in *Gaia* DR3 with declination $\delta > -30^\circ$ and apparent *Gaia* G -band magnitude $G < 17$. The upper right panel displays the sample of ellipsoidal variables with apparent magnitude $G < 17$. The lower left panel displays all the ellipsoidal variables in our vetted sample (i.e., objects with well-constrained distances and well-sampled ZTF light curves) colored by minimum mass ratio. The lower right panel shows our final set of observed targets (red) and objects that were either rejected after inspection of their light curves or not observed (yellow). Note that a significant fraction of all candidates are above the main-sequence, as expected for luminous binaries. Our follow-up prioritized objects near the main-sequence, which are more likely to host dark companions.

3.2 Follow-up Strategy

We obtained follow-up spectra at multiple epochs using spectrographs at Palomar and Keck Observatories, with the goal of measuring multi-epoch radial velocities (RVs) with a target precision of $\approx 10 \text{ km s}^{-1}$ at $G = 17$. Since the expected epoch-to-epoch RV shifts for a close BH or NS companion are large ($\gtrsim 100 \text{ km s}^{-1}$), this modest RV precision is sufficient to test the hypothesis that the targets have a BH or NS companion.

We mainly relied on the Double Spectrograph (DBSP; [Oke & Gunn 1982](#)) on the Palomar 200-inch telescope. Observing on the red and blue arms simultaneously, we used a 1.0, 1.5, or 2.0 arcsec slit (depending on seeing conditions) to obtain spectra over a total wavelength range of 3500 Å to 8000 Å with a typical spectral resolution $R \approx 2000$. Data reduction (i.e. bias and flat field correction, cosmic ray removal, wavelength calibration, sky subtraction, extraction of 1D spectra, and heliocentric RV corrections) was performed using Pypelt ([Prochaska et al. 2020](#)).

We also observed some targets using the Low Resolution Imaging Spectrometer (LRIS; [Oke et al. 1995](#)) and the Echelle Spectrograph and Imager (ESI; [Sheinis et al. 2002](#)) at Keck. For these instruments, data reduction was performed using the LRIS automated reduction Pipeline (LPIPE; [Perley 2019](#)) and the MAuna Kea Echelle Extraction (MAKEE) pipeline, respectively. A log of all of our observations can be found in Table 1.

3.3 Flexure Corrections

The DBSP instrument hangs off of the back of the Hale telescope, and can thus move from epoch to epoch. This “flexure” can lead to changes in the wavelength solution between calibration arcs and science exposures, ultimately resulting in spurious radial velocities. A common strategy to minimize flexure is to take an arc lamp exposure on-sky immediately before or after observing each target. However, this approach significantly increases the required telescope time, and we found that even when arcs were taken immediately after each target, the inferred RVs of standard stars were only stable at the $\approx 30 \text{ km s}^{-1}$ level. We therefore used telluric absorption lines with known wavelengths as a reference instead. Specifically, we produced a telluric model spectrum with appropriate airmass for each observation from a grid of high-resolution models of telluric absorption spectra from the HITRAN2020 molecular spectroscopic database ([Gordon et al. 2022](#)).

We smoothed this template to the resolution of the observation assuming a Gaussian line spread function, and determined the radial velocity shift of the telluric template that minimized the χ^2 statistic with respect to the observed spectrum (see Equation 1) within a wavelength range of 7585 Å to 7650 Å (which contains the A-band of molecular oxygen and is commonly used for telluric wavelength calibrations; e.g. [Chubak et al. 2012](#)). This allowed us to calculate flexure corrections as a pre-processing step before applying heliocentric corrections and measuring RVs at each epoch. Once our flexure

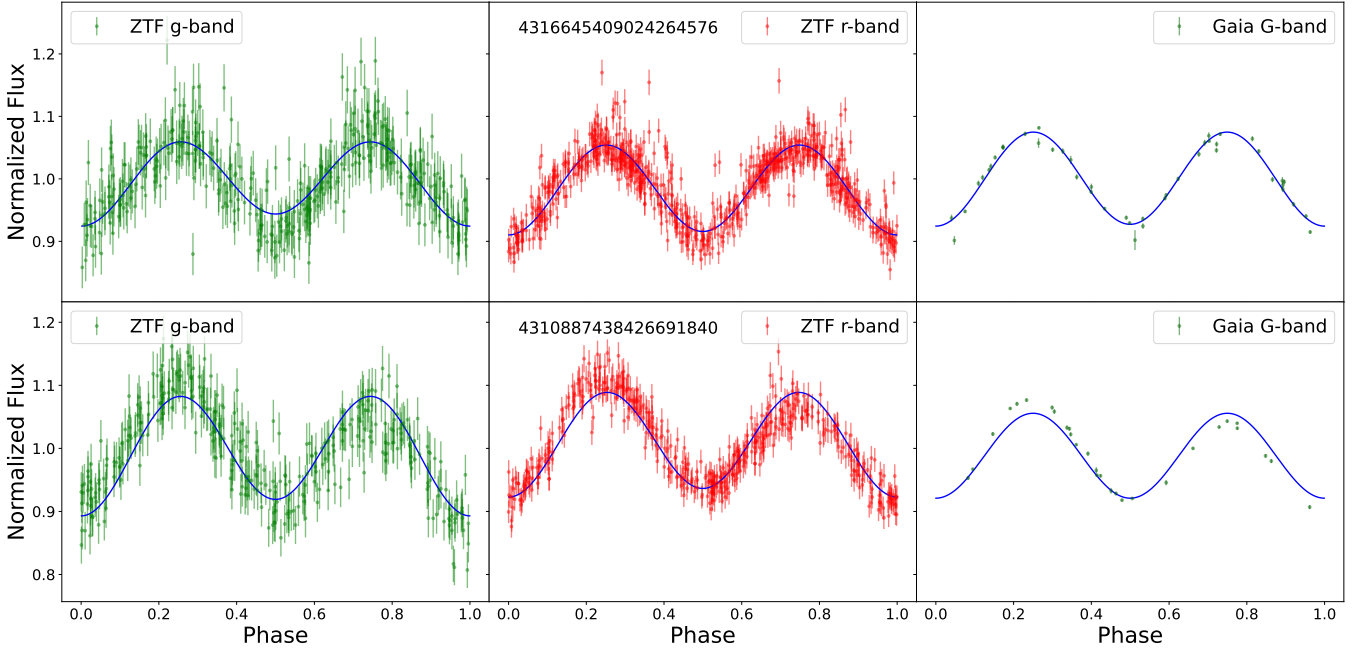


Figure 2. Comparison of light curve data in ZTF *g*-band, ZTF *r*-band, and *Gaia* *G*-band for ellipsoidal variables. Top Row: Light curves for typical ellipsoidal variable candidate with *Gaia* DR3 ID 4316645409024264576. Bottom Row: Light curves for anomalous ellipsoidal variable candidate with *Gaia* DR3 ID 4310887438426691840, rejected due to significant difference between light curve maxima (a signature of the “O’Connell Effect”, e.g. see O’Connell 1951 and Pribulla et al. 2011). A summary of our reasons for the rejection of candidates with $\hat{q}_{\min} > 0.8$ which otherwise satisfy our automated selection criteria can be found in Appendix A. Details on our best-fit light curves (which model ellipsoidal variability as the sum of Fourier harmonics) can be found in Appendix C. For these targets and many other in our sample, the ZTF light curves are better-sampled than the relatively sparse *Gaia* light curves, but the *Gaia* light curves have higher SNR.

corrections were applied, the inferred RVs of standard stars were generally consistent within 10 km/s. We present an example of our flexure correction method in Figure 3. Our flexure correction method was only necessary for DBSP; we found that the ESI RVs were stable, and that the flexure correction built into LPipe (which uses sky emission lines) worked well for the LRIS observations.

4 ANALYSIS

4.1 Radial Velocity Measurements

We used theoretical grids provided by Pecaut & Mamajek (2013) to estimate the spectral type and effective temperature of each primary star based on its $G_{BP} - G_{RP}$ color. We retrieved the appropriate BOSZ Kurucz model spectrum for each target (with appropriate instrumental broadening) from the STSCI Archive (Bohlin et al. 2017). Since our candidates are all rapidly rotating, there are not many strong metal lines in their observed spectra. Hence, we assumed a solar metallicity for all model spectra; nevertheless, our results are not strongly sensitive to this choice. Adopting a linear limb darkening coefficient of 0.5, we then used the `rotBroad` function from PyAstronomy (Czesla et al. 2019), which implements the formulae in Gray (1992), to apply rotational broadening to the model spectra assuming a projected rotation velocity $v \sin i = 2\pi R/P$. Here, the radius was assumed to follow a typical main sequence mass-radius relation given by $(M/M_{\odot}) = (R/R_{\odot})^{0.8}$ for $M < 1 M_{\odot}$ and $(M/M_{\odot}) = (R/R_{\odot})^{0.57}$ for $M \geq 1 M_{\odot}$, and the mass was inferred from the absolute *G*-band magnitude (see Section 4.3). We found that this rotational broadening was typically on the order of $v \sin i \sim 100 \text{ km s}^{-1}$. The result of this procedure was a template

spectrum with absorption lines that had a similar depth and width to the observed spectra.

To determine the best fit radial velocity, we found the minimum of the χ^2 statistic between the shifted template spectrum and observation as a function of radial velocity. The chi-squared statistic is defined to be:

$$\chi^2 = \sum_{\lambda} \frac{(f_{\text{template},\lambda} - f_{\text{obs},\lambda})^2}{\sigma_{\lambda}^2} \quad (1)$$

where $f_{\text{template},\lambda}$ is the flux of the template spectrum, $f_{\text{obs},\lambda}$ is the flux of the observed spectrum, and σ_{λ} is the uncertainty in the flux of the observed spectrum at wavelength λ , respectively. Note that flexure corrections were subtracted from our determined radial velocity to achieve the final RV measurement at a particular epoch. We repeated this procedure for each epoch for each ellipsoidal variable.

We provide example spectral fits for a DBSP (i.e. low-resolution) observation and an ESI (higher-resolution) observation of a candidate ellipsoidal variable in Figure 4. We compare the two spectral fits over wavelength ranges which include either the $H\alpha$ line (i.e. 6000 Å - 6600 Å) or the Ca triplet (i.e. 8400 Å - 8900 Å). After testing both the stability of our RV determinations and the relative strength of the signals, we decided to rely on the $H\alpha$ line and Ca triplet for RV determination in DBSP/LRIS and ESI observations, respectively. In most cases, we found the the template spectra to match the shape of the observed spectra reasonably well. In a few cases, we found via visual inspection that the spectral model did not yield a reliable fit in the default spectral region (i.e. $H\alpha$ or Ca triplet) due to data artifacts and/or an imperfect choice of template. In these cases, we used the other spectral region instead, regardless of instrument. A

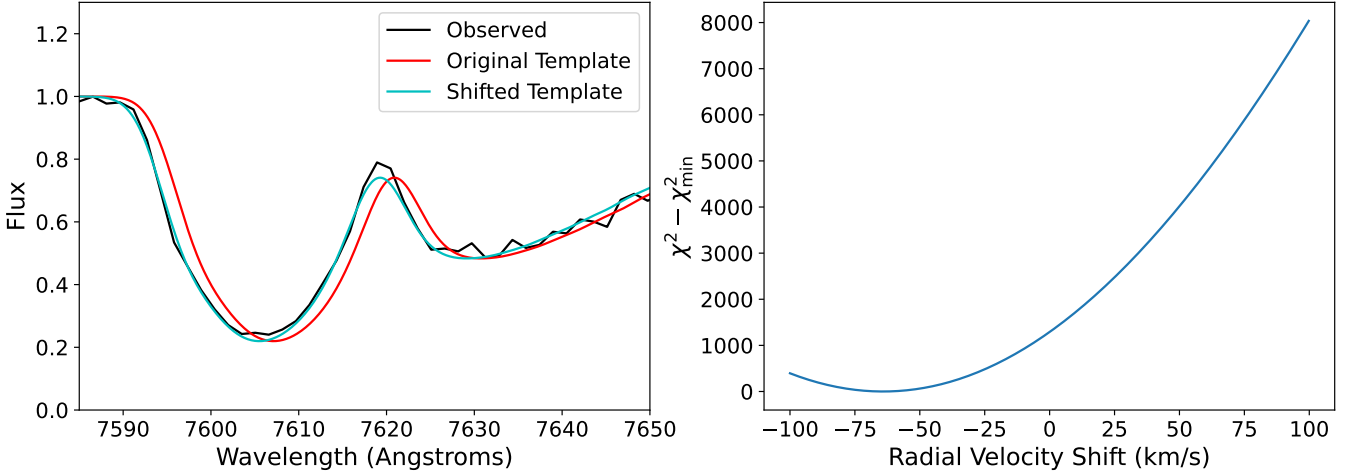


Figure 3. Determination of flexure correction for DBSP observation of ellipsoidal variable candidate with *Gaia* DR3 ID 2062434366319612672 at UTC epoch 2022-08-25 07:48:34. The left panel shows the effect of applying the determined flexure correction to the template spectrum; we see that the telluric line in the shifted template better matches the telluric line in the observed spectrum. The right panel shows the chi-squared value as a function of radial velocity shift. The minimum of the chi-squared curve was identified as the inferred flexure correction, which is -64 km s^{-1} at this epoch. Flexure corrections significantly improved the stability of our RV measurements.

few observed spectra showed hints of line splitting and/or epoch-to-epoch changes in line profile, which are most likely due to a luminous secondary. We did not attempt to account for these variations when inferring RVs. We provide a summary of all of our RV measurements in Table 1. The reported RV uncertainties are based on observations of standard stars with the same instrumental setup; in all cases, we adopt an uncertainty of 10 km s^{-1} for DBSP and LRIS observations, and 5 km s^{-1} for ESI observations.

4.2 Radial Velocity Fits

We fit for the semi-amplitude K and center-of-mass radial velocity γ based on a sinusoidal function:

$$RV(t) = \gamma - K \sin\left(\frac{2\pi(t - T_0)}{P}\right) \quad (2)$$

This model assumes that the orbit is circular, which is justified, since ellipsoidal binaries undergo tidal interactions that both circularize the orbit and synchronize the rotational and orbital periods (Zahn 1977; Lurie et al. 2017). The orbital period P is fixed to the value from the *Gaia* DR3 catalog, while the epoch of conjunction T_0 is determined from the ZTF light curve in the *g*-band (see Appendix C for details). Since there are two free parameters, we only analyzed variables with at least two RV measurements.

In general, we expect that $K \geq 0$. If we instead inferred $K < 0$ from our initial fit, then we took this as an indication that our assumed T_0 was inaccurate by half a period (i.e. the deeper minimum of the ZTF *g*-band light curve does not actually correspond to the true epoch of conjunction). While this could physically occur due to, e.g., a large spot on the side of the luminous component that faces away from an unseen massive companion, it is more likely that the uncertainty in the value of T_0 is simply a consequence of the light curve minima having similar depths. In such cases, spectroscopic follow-up is necessary to provide further information and help identify the epoch of conjunction. Candidates for which we shifted T_0 by half a period are indicated using an asterisk in Appendix C.

To fit this model to the observed RVs, we performed MCMC sam-

pling with the *emcee* package (Foreman-Mackey et al. 2013). We used uniform priors over a wide range of possible values, restricting $|\gamma| < 500$ and $0 < K < 1000$. The likelihood compares measured and predicted RVs assuming Gaussian uncertainties. We randomly initialized 100 walkers and sampled the posterior for 1000 iterations. We report the median and middle 68% of the posterior samples for both quantities in Table 2. In cases where we only have two measurements, the RV curves may not be well-constrained, and the error bars on our estimates of the companion mass reflect this uncertainty. Even in these cases, the measured RVs are – when combined with the photometric ephemeris – strongly inconsistent with a companion mass $\gtrsim 1 M_\odot$, and thus make it unlikely that the companions are neutron stars or black holes.

We show two examples of radial velocity curves, along with their corresponding observations (color-coded by instrument used), in Figure 5. The left panel shows an RV curve with a typical number of observations, while the right panel shows one of the targets for which we obtained the largest number of observations. Figure D1 in the appendix shows similar RV curves for all the objects in our follow-up sample. In general, we infer relatively small RV semi-amplitudes; the median value is about 17 km s^{-1} , and the maximum value is about 61 km s^{-1} . A few outlier data points are most likely due to systematic errors due to luminous secondaries changing the shape of spectral lines between epochs.

4.3 Companion Masses

We estimated the primary star mass, M_1 , from its *G*-band absolute magnitude using the empirical *G*-band mass-luminosity relationship for main-sequence stars from Janssens et al. (2022). Then, given the orbital period P , semi-amplitude K , and an assumed inclination i , the companion mass M_2 can be found by numerically solving the following equation:

$$K = \left(\frac{2\pi G}{(M_1 + M_2)^2 P} \right)^{1/3} M_2 \sin i \quad (3)$$

We infer minimum companion masses by assuming an inclination

Table 1. Summary of radial velocity measurements for vetted sample of ellipsoidal variables.

<i>Gaia</i> Source ID	Observation Time (HJD)	Radial Velocity (km s ⁻¹)	Instrument
2033460169042378752	2459818.8998	26±10	LRIS
2033460169042378752	2460084.8948	8±10	DBSP
2033460169042378752	2460055.9840	57±10	DBSP
2033460169042378752	2459824.8937	37±5	ESI
2033460169042378752	2459818.9928	55±10	LRIS
1342190925113500416	2459980.0472	-16±10	DBSP
1342190925113500416	2460055.9698	-23±10	DBSP
1342190925113500416	2459967.0470	-65±10	DBSP
3396537760623971328	2459878.1285	12±5	ESI
3396537760623971328	2459877.9158	12±5	ESI
3396537760623971328	2459878.0306	22±5	ESI
4277589209792837632	2459813.7896	-97±10	DBSP
4277589209792837632	2460055.8814	-105±10	DBSP
4277589209792837632	2460084.8819	-106±10	DBSP
4277589209792837632	2459813.6924	-93±10	DBSP
2057298203894617088	2459813.8107	-25±10	DBSP
2057298203894617088	2459877.7123	-58±5	ESI
2057298203894617088	2459851.6926	6±10	DBSP
2057298203894617088	2459813.9245	-43±10	DBSP
2211471926201876992	2459877.7954	-93±5	ESI
2211471926201876992	2459877.9057	-113±5	ESI
4316645409024264704	2460084.9442	-54±10	DBSP
4316645409024264704	2459873.7367	2±10	DBSP
4316645409024264704	2459813.8025	-5±10	DBSP
4316645409024264704	2459813.7065	-3±10	DBSP
188218592331364736	2459970.6299	-13±10	DBSP
188218592331364736	2459969.6031	22±10	DBSP
188218592331364736	2459878.1472	12±5	ESI
188218592331364736	2459878.0710	22±5	ESI
188218592331364736	2459877.8848	22±5	ESI
188218592331364736	2459851.8790	11±10	DBSP
188218592331364736	2459847.1070	3±10	LRIS
188218592331364736	2459819.1302	8±10	LRIS
188218592331364736	2459818.1245	6±10	LRIS
4305376170746099712	2460055.9377	-47±10	DBSP
4305376170746099712	2459816.9013	-58±10	DBSP
4305376170746099712	2459816.8212	-28±10	DBSP
3456522854428709888	2459971.8484	34±10	DBSP
3456522854428709888	2459851.8872	15±10	DBSP
3456522854428709888	2459818.1288	8±10	LRIS
3456522854428709888	2459819.1384	26±10	LRIS
3456522854428709888	2459878.0885	12±5	ESI
3456522854428709888	2459877.9523	42±5	ESI
3456522854428709888	2459874.0142	57±10	DBSP
3457961423656077312	2459815.9623	0±10	DBSP
3457961423656077312	2459847.1222	13±10	LRIS
3457961423656077312	2459877.8933	-2±5	ESI
3457961423656077312	2459878.0804	-58±5	ESI
3457961423656077312	2459813.9804	-52±10	DBSP
2163873350591724032	2459817.8809	-71±10	LRIS
2163873350591724032	2459818.8784	-63±10	LRIS
2163873350591724032	2459824.8820	63±5	ESI
2163873350591724032	2459877.7848	42±5	ESI
2062434366319612672	2459816.8319	16±10	DBSP
2062434366319612672	2459816.9133	-62±10	DBSP
2062434366319612672	2459877.7710	-73±5	ESI
2062434366319612672	2459873.7703	29±10	DBSP
4310698008860121088	2459846.8681	18±10	LRIS
4310698008860121088	2459877.7400	27±5	ESI
4310698008860121088	2460084.9352	17±10	DBSP

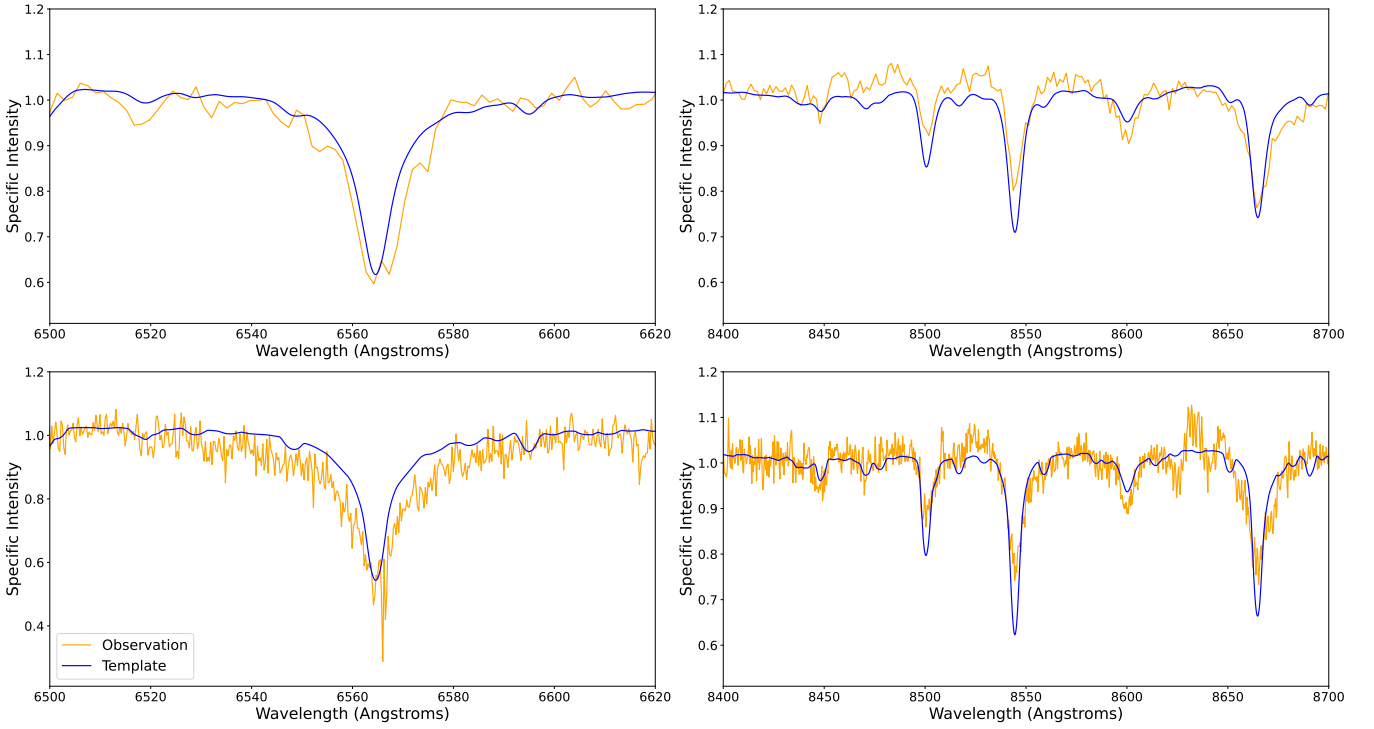


Figure 4. Example spectral fits for a DBSP observation and an ESI observation of ellipsoidal variable with *Gaia* DR3 ID 2062434366319612672. In both cases, we choose wavelength ranges for template fitting to emphasize the prominent signals due to the $H\alpha$ line and the Ca triplet. The agreement between the data and the model is not perfect, but is sufficient for robust measurement of radial velocities.

Table 2. Derived companion masses for vetted sample of ellipsoidal variables, assuming an inclination of 90° . Note that \hat{q}_{\min} is the modified minimum mass ratio reported by [Gomel et al. \(2021a\)](#), and is not what we derived based on our radial velocity measurements.

<i>Gaia</i> Source ID	Period (days)	T_0 (HJD)	γ (km s $^{-1}$)	K (km s $^{-1}$)	M_1 (M_\odot)	$M_{2,\min}$ (M_\odot)	\hat{q}_{\min}
2033460169042378752	0.270854 ± 0.000057	2458206.1367 ± 0.0012	41^{+4}_{-4}	22^{+6}_{-6}	1.14 ± 0.11	$0.07^{+0.02}_{-0.02}$	0.91 ± 0.22
1342190925113500416	0.279545 ± 0.000078	2458204.9995 ± 0.0008	-31^{+6}_{-6}	17^{+6}_{-7}	0.97 ± 0.09	$0.05^{+0.02}_{-0.02}$	0.52 ± 0.12
3396537760623971328	0.311336 ± 0.000074	2458205.7569 ± 0.0016	16^{+3}_{-3}	7^{+4}_{-4}	1.11 ± 0.11	$0.02^{+0.01}_{-0.01}$	0.69 ± 0.17
4277589209792837632	0.329189 ± 0.000082	2458206.0749 ± 0.0014	-100^{+5}_{-5}	8^{+5}_{-5}	1.49 ± 0.14	$0.04^{+0.02}_{-0.02}$	1.18 ± 0.34
2057298203894617088	0.352784 ± 0.000096	2458207.0088 ± 0.0011	-5^{+8}_{-8}	52^{+9}_{-10}	1.25 ± 0.12	$0.22^{+0.04}_{-0.05}$	1.01 ± 0.26
2211471926201876992	0.353515 ± 0.000108	2458230.0924 ± 0.0011	-99^{+4}_{-4}	14^{+5}_{-5}	1.28 ± 0.12	$0.06^{+0.02}_{-0.02}$	0.82 ± 0.20
4316645409024264704	0.390803 ± 0.000094	2458207.0437 ± 0.0018	-10^{+5}_{-5}	16^{+6}_{-6}	1.77 ± 0.78	$0.08^{+0.04}_{-0.05}$	1.01 ± 0.25
188218592331364736	0.395750 ± 0.000142	2458206.6547 ± 0.0011	15^{+2}_{-4}	5^{+3}_{-4}	1.04 ± 0.10	$0.02^{+0.01}_{-0.01}$	1.08 ± 0.27
4305376170746099712	0.409171 ± 0.000104	2458279.0047 ± 0.0027	-39^{+6}_{-7}	17^{+9}_{-9}	1.25 ± 0.12	$0.07^{+0.04}_{-0.04}$	1.07 ± 0.29
3456522854428709888	0.430926 ± 0.000134	2458205.7704 ± 0.0009	32^{+3}_{-3}	21^{+4}_{-4}	1.32 ± 0.13	$0.09^{+0.02}_{-0.02}$	1.04 ± 0.27
3457961423656077312	0.458269 ± 0.000152	2458385.8186 ± 0.0022	-26^{+3}_{-3}	37^{+4}_{-4}	1.42 ± 0.14	$0.18^{+0.02}_{-0.02}$	1.14 ± 0.28
2163873350591724032	0.481034 ± 0.000174	2458303.9553 ± 0.0032	-8^{+4}_{-4}	61^{+4}_{-4}	2.06 ± 0.08	$0.41^{+0.03}_{-0.03}$	1.04 ± 0.26
2062434366319612672	0.721862 ± 0.000404	2458207.1999 ± 0.0012	-33^{+4}_{-4}	44^{+4}_{-4}	1.76 ± 0.77	$0.30^{+0.03}_{-0.10}$	1.06 ± 0.26
4310698008860121088	0.751384 ± 0.000436	2458205.9044 ± 0.0043	32^{+6}_{-7}	17^{+11}_{-12}	2.20 ± 0.09	$0.12^{+0.08}_{-0.10}$	1.62 ± 0.46

of 90° degrees. For randomly oriented orbits, the expected median inclination is 60° degrees. The typical inclination for objects in our sample may differ from this value: relatively edge-on orbits may be favored by the selection of large variability amplitudes, but the most edge-on orbits may be excluded because (for luminous companions) they would show eclipses. Figure 6 shows how the inferred companion mass for a typical object in our sample depends on the assumed inclination for a fixed value of K . The error bars represent a 2σ confidence interval derived based on the uncertainty in the primary mass. We observe that the inferred companion mass increases with decreasing inclination, with the inferred M_2 at a typical inclination of 60° only differing slightly from the minimum inferred mass. Only

for nearly face-on inclinations, which are geometrically improbable, does the actual companion mass exceed the minimum by more than a factor of two. In fact, while the observed RV semi-amplitude would imply a companion mass higher than $1 M_\odot$ for inclination $i < 25^\circ$, such a low inclination would also result in a smaller photometric variability amplitude than exhibited by the observed systems (see simulations in Section 5.1).

To provide a summary of our results in Table 2, we plot the inferred companion mass versus period and primary mass for an inclination of 90° in Figure 7. There is a weak trend of increasing companion mass with longer periods and higher primary masses. Our median inferred companion mass is about 0.08 solar masses; if we assume an

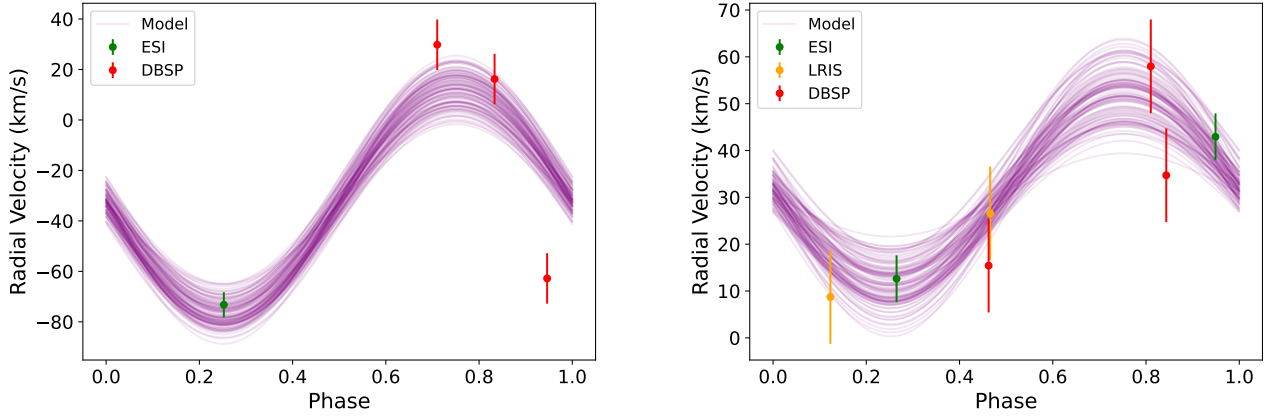


Figure 5. Left Panel: Radial velocity curve for ellipsoidal variable candidate with *Gaia* DR3 ID 2062434366319612672. The inferred RV semi-amplitude is 44 km s^{-1} . Right Panel: Radial velocity curve for ellipsoidal variable candidate with *Gaia* DR3 ID 3456522854428709632. The inferred RV semi-amplitude is 21 km s^{-1} . In both panels, we plot fitted RV curves corresponding to 100 random samples of (γ, K) from the posterior. Similar fits for all 14 variables are shown in Figure D1.

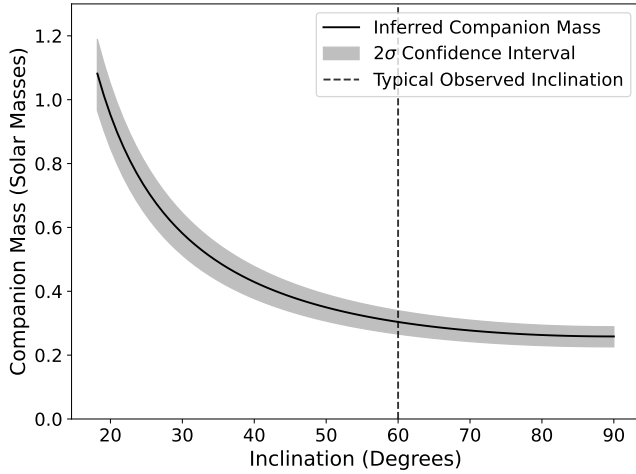


Figure 6. Dependence of derived companion mass (given the observed period and RV semi-amplitude) on inclination for ellipsoidal variable candidate with *Gaia* DR3 ID 3457961423656077056. Although the companion mass could in principle be large for a sufficiently face-on inclination, a typical inclination of 60° implies a companion mass of only $0.3 M_\odot$.

inclination of 60° , we infer a median companion mass of 0.09 solar masses instead. The implications of this are discussed in Section 5.

5 DISCUSSION

Our spectroscopic follow-up of the most promising ellipsoidal variables in the sample selected from *Gaia* DR3 by Gomel et al. (2022) revealed a population of binaries with mass ratios much less than unity, contrary to expectations. Hence, we must reject the hypothesis that these binaries are ellipsoidal variables hosting massive dark companions. We now consider four alternative explanations for the objects' photometric variability.

(i) The sources are indeed ellipsoidal variables with dark companions, but the companions have low masses ($M_2 \sim 0.2 M_\odot$). We

consider this unlikely: it is not clear what the low-mass dark secondaries would actually be, and their mass ratios are in any case not large enough to explain the observed variability through tidal deformation of the primary alone.

(ii) The sources are actually detached binaries with a low-mass, luminous secondaries (i.e., main-sequence stars).

(iii) The sources are actually contact binaries (meaning that two luminous components share a common envelope), with an extreme mass ratio, and possibly with spots on either component.

(iv) The sources are not binaries at all, but rotational or pulsating variables whose light curves just happen to mimic ellipsoidal variability.

We explore the expected light curves and RV amplitudes for plausible luminous binary scenarios below using PHOEBE (Wilson & Devinney 1971; Prša & Zwitter 2005; Conroy et al. 2020), which models the light curves and RVs of close binaries.

5.1 PHOEBE Light Curve Models

We used PHOEBE to calculate model light curves and RV curves by specifying the mass ratio, orbital period, inclination, semi-major axis, primary and secondary radii, and primary and secondary temperatures as input parameters. The semi-major axis was self-consistently determined based on the primary mass, secondary mass, and orbital period. We investigated four different models, all with a primary mass of $1 M_\odot$, a primary temperature of 6000 K , and an orbital period of 0.5 days. For each possible scenario, we adjusted parameters such as the inclination, component radii, and spot morphology (where applicable) to produce light curves similar to the observed light curves in our sample. We show predicted light curves and primary RVs for four models in Figure 8; the corresponding meshes are shown in Figure 9. The models are as follows:

(i) A default ellipsoidal binary with a secondary mass of $2 M_\odot$ (i.e. $q = 2.0$) at an observed inclination of 60° . In this case, we set the radius of the primary to 0.99 times the effective Roche lobe radius. We also set the radius of the secondary to a vanishingly small value to mimic an unseen massive companion. This is the scenario corresponding to a true BH/NS companion. It predicts a

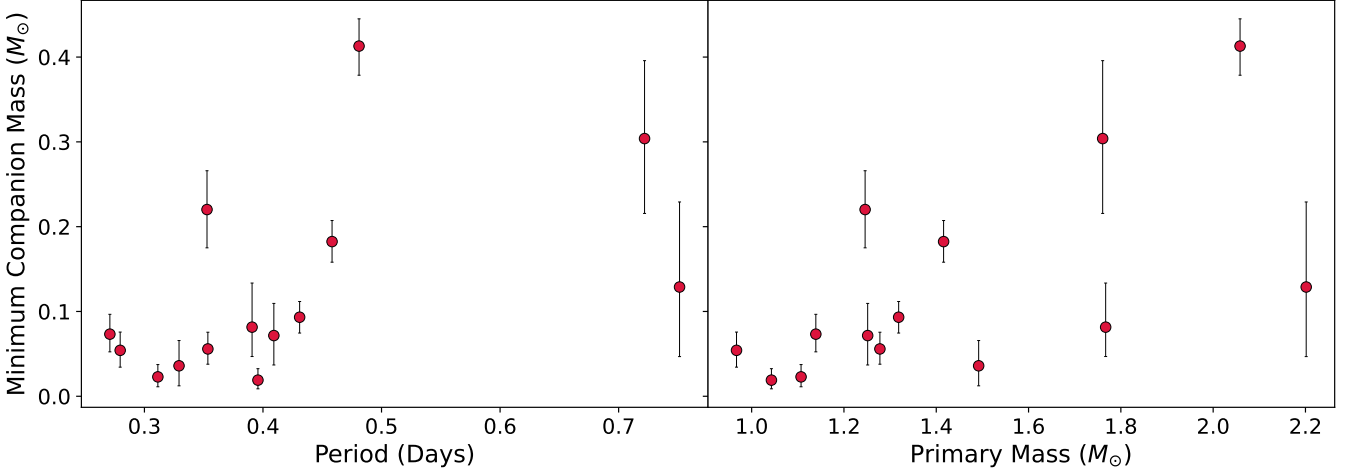


Figure 7. Left Panel: Derived minimum companion mass as a function of period. Right Panel: Derived companion mass as a function of primary mass. Our assumed inclination is 90° . Most of our inferred companion masses are near $0.1 M_{\odot}$ – much lower than expected for any compact object companion. We do not observe a strong trend with either orbital period or primary mass.

light curve with uneven minima and photometric variability on half of the orbital period. The corresponding radial velocity curve has a semi-amplitude greater than 200 km s^{-1} , much larger than any of our observed binaries.

(ii) A detached binary with a low-mass luminous secondary of mass $0.2 M_{\odot}$ (i.e. $q = 0.2$) at an observed inclination of 60° . In this case, we set the radius of the primary to 0.99 times the effective Roche lobe radius. We also set the radius of the secondary to $0.2 R_{\odot}$ and the temperature of the secondary to 4000 K, as appropriate for a low-mass main sequence star. While the light curve still displays the typical ellipsoidal features described above, it has a smaller variability amplitude. On the other hand, the corresponding radial velocity curve has a semi-amplitude less than 50 km s^{-1} , in accordance with our observations.

(iii) A contact binary with a low-mass luminous secondary of mass $0.2 M_{\odot}$ (i.e. $q = 0.2$) at an observed inclination of 45° . In this case, we set the radius of the primary to 1.09 times the effective Roche lobe radius. While we did not specify the radius of the secondary (as it is no longer a free parameter), we did set the temperature of the secondary to 6000 K (as we expect the components to be in thermal equilibrium). In this case, the radial velocity curve maintains a small semi-amplitude, but the light curve displays a lack of unequal minima.

(iv) A spotted contact binary with a low-mass luminous secondary of mass $0.2 M_{\odot}$ (i.e. $q = 0.2$) at an observed inclination of 45° . Once again, we set the radius of the primary to 1.09 times the effective Roche lobe radius, and the temperature of the secondary to 6000 K. However, we also added a spot of temperature 4500 K and an angular radius of 30° at a co-latitude of 90° and a longitude of 180° with respect to the spin axis. The location of the spot was chosen to produce uneven minima in the observed light curve. Of course, this is not the only configuration of spots that could produce apparent ellipsoidal variability: a spot of a different angular radius and effective temperature or the addition of another spot with different physical characteristics on the opposing end of the binary would also produce observed ellipsoidal modulation, albeit with a different variability amplitude. However, we decided not to consider scenarios involving multiple spots for the sake of simplicity.

We observe that our base case hypothesis (i.e. an ellipsoidal vari-

able with $q = 2.0$) produces a typical ellipsoidal light curve with a large RV semi-amplitude. The light curve matches our observations, but the radial velocity curve does not. On the other hand, both a detached binary with $q = 0.2$ and a contact binary with $q = 0.2$ produce observed RV curves with small semi-amplitudes that match our observations. In the scenario of a contact binary with a spotted secondary, the light curve still displays a characteristic difference in minima that matches our observations; this is because the spot mimics the effects of gravity darkening in an ellipsoidal binary (a “reverse” O’Connell effect, see O’Connell 1951). While the spotted contact binary seems to match our observed data the best, it is also the most complicated model.

5.1.1 Extreme mass ratio contact binaries

Due to mass transfer, magnetic braking, and thermal relaxation oscillations, the mass ratio of a contact binary evolves towards small values until it reaches a critical threshold (Eggleton 2012). At this threshold, the Darwin instability will cause a runaway loss of angular momentum that leads to a coalescence (Eggleton 2012). Recent studies of observed samples of contact binaries have modeled the mass ratio distribution of contact binaries as a function of orbital period, and have found that extreme mass ratio contact binaries (i.e. $q \sim 0.2$) are not uncommon at the typical periods ($P \sim 0.3$ days) in our sample (Kobulnicky et al. 2022; Pešta & Pejcha 2022). We thus suspect that (spotted) contact binaries are among the most common false-positives in the *Gaia* sample.

5.1.2 Evidence of spots in the phased light curves

To check for long-timescale variations in the ZTF light curves that could be caused by spots moving on stellar surfaces, we divided the data for each target in our sample into two segments of equal length and visually searched for changes in phase, amplitude, or shape between the two segments. In a few sources, we did find evidence of the phased light curve shape evolving in a manner consistent with spot activity. A majority of the objects in the sample did not display convincing evidence of light curve shape evolution. We provide ex-

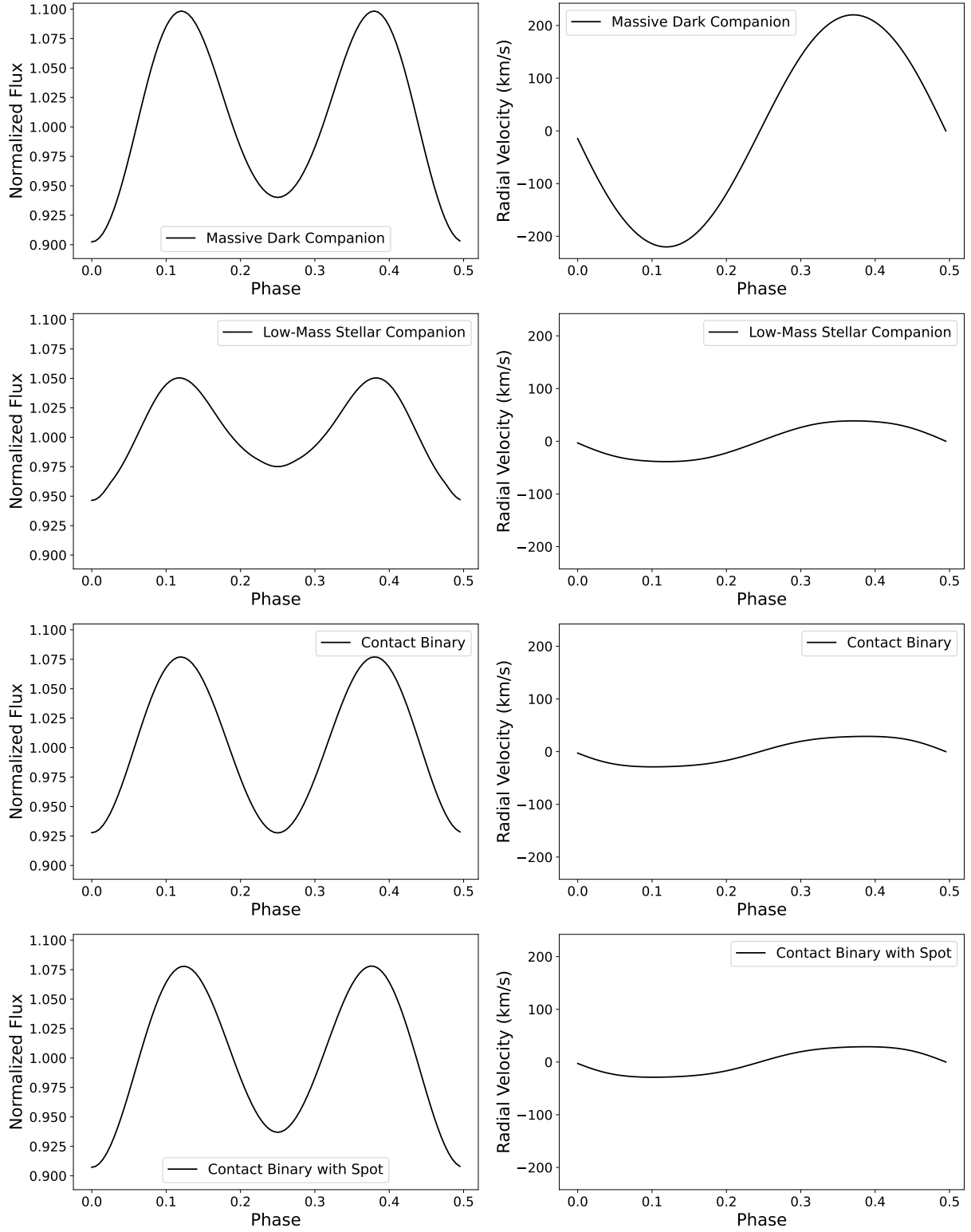


Figure 8. Row One: Simulated light curve and RV curve for a $q = 2.0$ ellipsoidal variable with a massive dark companion (assuming an inclination of 60°). Row Two: Simulated light curve and RV curve for a detached binary with $q = 0.2$ (assuming an inclination of 60°). Row Three: Simulated light curve and RV curve for a contact binary with $q = 0.2$ (assuming an inclination of 45°). Row Four: Simulated light curve and RV curve for a spotted contact binary with $q = 0.2$ (assuming an inclination of 45°). We find that only a contact binary with a spot can reproduce the large variability amplitude, “ellipsoidal” light curve shape, and low RV semi-amplitude characteristic of our observations.

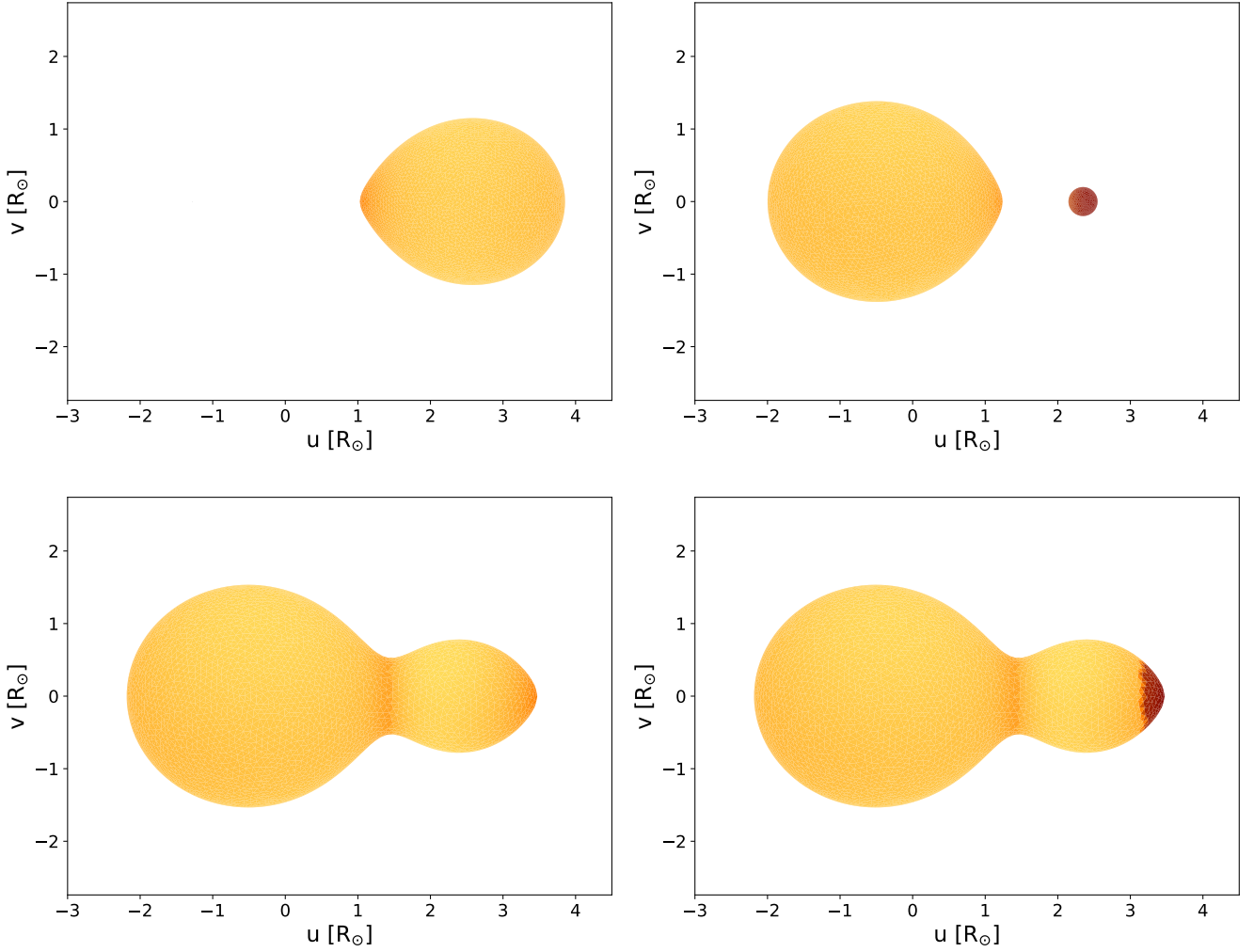


Figure 9. Top Row: Visualization of a $q = 2.0$ ellipsoidal variable with a massive dark companion and a $q = 0.2$ detached binary with a low mass secondary (assuming an inclination of 60°). Bottom Row: Visualization of a $q = 0.2$ extreme mass ratio contact binary with and without a spot (assuming an inclination of 45°). In both cases, the mesh is colored by effective temperature.

amples of ZTF g -band light curves with and without long-timescale variations in Figure 10.

The fact that some objects in our sample show evidence of spot evolution supports the hypothesis that spots contribute to the observed variability in at least some of the sample. Spot evolution timescales in close binaries can span decades (e.g. [Eaton & Hall 1979](#)), so the lack of detected light curve evolution in most of the targets does not preclude spots.

5.2 Single Star Scenarios

We now consider possible scenarios in which the sources are not binaries at all, but just single variable stars with light curves that serendipitously resemble ellipsoidal variables. One such plausible case is a rotating single-star with spots that generate photometric variability on the rotational period. Another potential scenario is a pulsating variable star; however, pulsations are unlikely due to the observed rapid rotation ($v \sin i \sim 100 \text{ km s}^{-1}$), and lack of known astrophysical pulsations at these timescales and amplitudes in this part of the CMD. More convincingly, the fact that most of the objects in the sample are above the main-sequence suggests binarity, as

it is improbable that a single star could produce the observed over-luminosity. In the end, it is important to note that there could be more than one type of contaminant in the sample of candidate ellipsoidal variables.

5.3 Completeness of our follow-up

We observed 14 candidates on the main sequence of the extinction-corrected *Gaia* CMD, prioritizing bright sources with large photometrically-inferred minimum mass ratios. While this represents a small fraction of the 6306 candidates selected by [Gomel et al. \(2022\)](#), we expect that the false-positive rate in our spectroscopic follow-up sample is *lower* than in the full [Gomel et al. \(2022\)](#) sample because we excluded (a) sources above the main-sequence, which are likely luminous binaries and (b) sources with ZTF light curves displaying systematic deviations from ellipsoidal variability. Only one of the objects in our spectroscopic sample (*Gaia* DR3 ID 4310698008860121216) is among the 262 candidates identified by [Gomel et al. \(2022\)](#) that had inferred mass ratios larger than unity at the 1σ level. However, the majority of these 262 candidates lie above the main sequence in the extinction-corrected *Gaia* CMD, and

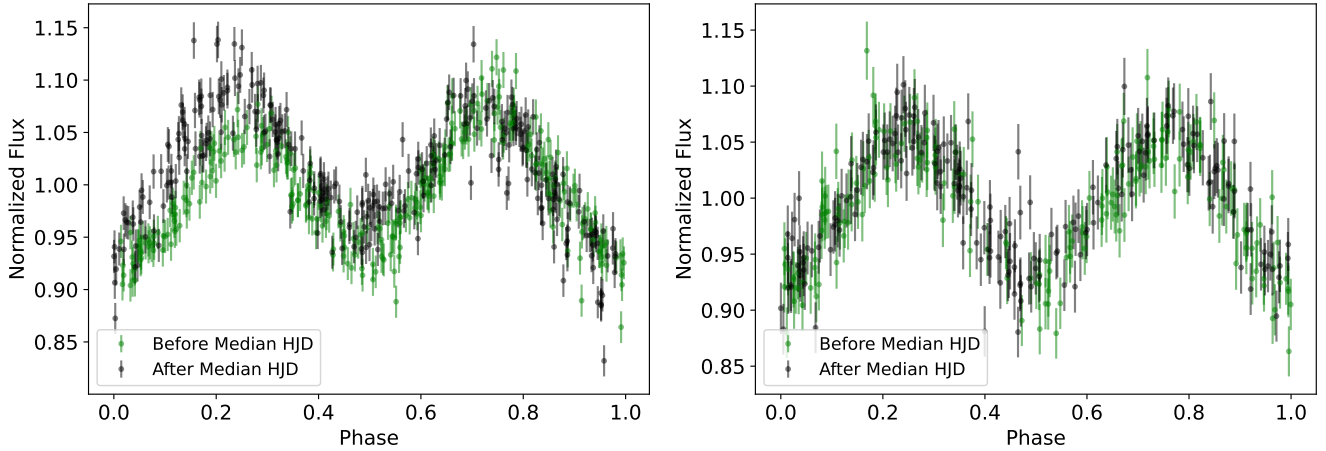


Figure 10. Phased ZTF *g*-band light curves for two objects from our sample. In both panels, we split the light curve into two sections, each corresponding to ≈ 2 years. In the left panel (*Gaia* DR3 ID 1342190925113500416), there is clear evolution of the light curve morphology between the two sections, a telltale sign of spot evolution. In the right panel (*Gaia* DR3 ID 4318115181190923392), the light curve is stable. This does not rule out spots, but it suggests that there was little spot evolution over ~ 4 years.

hence were excluded from our final sample. In any case, the minimum mass ratios inferred from the RV curves for the 14 candidates in our sample do not match the \hat{q}_{\min} values inferred from the variability amplitudes of the light curves. There is little reason to expect the photometrically-inferred minimum mass ratios to be any more reliable for the sources with the highest \hat{q}_{\min} values, particularly since sources with genuinely dark companions are astrophysically rare. Based on the “success rate” of 0/14 within our spectroscopic follow-up sample, a conservative lower limit on the false-positive rate for the full catalog is $\gtrsim 90\%$.

5.4 Challenges of using the mMMR in searches for compact object companions

The method suggested by Gomel et al. (2021a) is intended to search for objects that are close to completely filling their Roche lobe (i.e. $f \gtrsim 0.90$). However, this is a short-lived phase in the evolution of most binaries compared to evolutionary phases where both components are well within their Roche lobes or one component is completely Roche-lobe filling (e.g. Warner 2003). Hence, the population of observed binaries should primarily consist of binaries that are well detached (and not identifiable as hosting massive dark companions via the mMMR) or systems where the primary is already overflowing its Roche lobe. In fact, if a stellar mass BH companion was present in the latter case, we would expect such systems to be transient or persistent X-ray sources (though sources with long outburst recurrence times might not be easily detectable).

As a result, the central weakness of the method proposed by Gomel et al. (2021a) is that selection effects will cause a sample in which light curves display ellipsoidal modulation to be dominated by false positives. The most likely contaminants are close luminous binaries, which are more common than ellipsoidal variables with dark companions. In fact, among solar-type stars, about one out of every 200 sources is a binary with a period less than 1 day (e.g. El-Badry et al. 2022c). While the light curves of such binaries will often be distinguishable from those of ellipsoidal variables, their greater numbers and the ability of spots to distort light curves in nearly arbitrary ways make them a significant contaminant. However, single stars with rotational or pulsational variation can also serve as potential con-

taminants. While the sample curated by Gomel et al. (2022) could still contain stellar-mass BHs and NSs, a wider characterization of the sample (i.e. with a high degree of completeness) is required to further determine the sensitivity and specificity of their method.

6 CONCLUSION

We performed spectroscopic follow-up of 14 of the most promising variables in the *Gaia* DR3 sample of ellipsoidal variables curated by Gomel et al. (2022). In previous work, Gomel et al. (2021a) demonstrated that, under the assumption that all variability is indeed due to tidal deformation, a stringent lower limit on the mass ratio of an ellipsoidal variable can be inferred that is robust to assumptions about the mass, radius, and evolutionary state of the component stars. They termed this lower limit the “modified minimum mass ratio” (mMMR or \hat{q}_{\min}). Of the candidates in our sample, 12 had $\hat{q}_{\min} > 0.8$ and 10 had $\hat{q}_{\min} > 1.0$; however, we do not find any promising compact object companions. Our main conclusions are as follows:

- We selected our 14 targets based on their optical light curves, whose amplitude variability (when attributed entirely to a massive unseen companion) suggested that the secondary was a compact object (see Figure C1). All of these targets had apparent *Gaia* *G*-band magnitude ≤ 17 , well-constrained distances, available 3D dust map extinctions, and CMD positions on the main sequence (see Figure 1). We obtained spectra for each of these targets at at least 2 epochs, using the DBSP spectrograph as a primary tool (and the LRIS and ESI spectrographs at Keck as available). From the fitted semi-amplitudes of the RV curves (see Figure D1), we derive minimum companion masses of $\leq 0.5 M_{\odot}$ in all cases, rendering it unlikely that any of these binary systems host neutron stars or black holes (see Figure 7).
- We use PHOEBE modeling to explore detached systems with low-mass luminous secondaries and (spotted) contact binaries as alternative hypotheses for how binary systems with low mass ratios could produce the observed light curves (see Figures 8 and 9). We find that an extreme mass ratio contact binary with a spotted secondary can reproduce both an RV curve with a small semi-amplitude and a light curve with apparent ellipsoidal modulation.

• Since we selected candidates based on the position of the primary component relative to the main sequence on the *Gaia* CMD (which rules out Algol-type binaries) (see Figure 1), we conclude that the most common failure mode was probably mistaking a (spotted) contact binary for an ellipsoidal variable. We note that resource constraints restricted our investigation to a small subset of the original sample; there may still be stellar mass BHs in the dataset provided by Gomel et al. (2022). However, a significant fraction of their candidates can be eliminated right away based on their CMD position above the main sequence.

• Thus, further characterization of this sample (i.e. with a higher degree of completeness) is necessary to determine whether any BH/NS needles are hiding in the luminous binary haystack. All-sky, multi-epoch spectroscopic surveys such as SDSS-V (Kollmeier et al. 2017), which are capable of optical multi-object fiber spectroscopy, will be ideally suited to carry out this task. Spectroscopic follow-up of ellipsoidal binaries remains a promising avenue to understand the progenitors of low-mass X-ray binaries and characterize the population of dormant stellar mass black holes, but it must be approached with the assumption that a majority of light-curve selected candidates are false positives.

ACKNOWLEDGEMENTS

We thank the referee for a constructive report. We are grateful to Roy Gomel and Tsevi Mazeh for providing an early copy of their candidate list, Tsevi Mazeh for comments on an early draft of this manuscript, and the ZTF Variable Star Group for useful comments and discussions. This work made use of Astropy, a community-developed core Python package and an ecosystem of tools and resources for astronomy (Astropy Collaboration et al. 2018).

This work is based on observations obtained with the Samuel Oschin Telescope 48-inch and the 60-inch Telescope at the Palomar Observatory as part of the Zwicky Transient Facility project. ZTF is supported by the National Science Foundation under Grant No. AST-2034437 and a collaboration including Caltech, IPAC, the Weizmann Institute for Science, the Oskar Klein Center at Stockholm University, the University of Maryland, Deutsches Elektronen-Synchrotron and Humboldt University, the TANGO Consortium of Taiwan, the University of Wisconsin at Milwaukee, Trinity College Dublin, Lawrence Livermore National Laboratories, and IN2P3, France. Operations are conducted by COO, IPAC, and UW.

This work has made use of data from the European Space Agency (ESA) mission *Gaia* (<https://www.cosmos.esa.int/gaia>), processed by the *Gaia* Data Processing and Analysis Consortium (DPAC, <https://www.cosmos.esa.int/web/gaia/dpac/consortium>). Funding for the DPAC has been provided by national institutions, in particular the institutions participating in the *Gaia* Multilateral Agreement.

DATA AVAILABILITY

Data used in this study are available upon request from the corresponding author.

REFERENCES

Astropy Collaboration et al., 2018, *AJ*, **156**, 123
Bellm E. C., et al., 2019, *PASP*, **131**, 018002

- Bohlin R. C., Mészáros S., Fleming S. W., Gordon K. D., Koekemoer A. M., Kovács J., 2017, *AJ*, **153**, 234
Brown G. E., Bethe H. A., 1994, *ApJ*, **423**, 659
Chakrabarti S., et al., 2023, *The Astronomical Journal*, **166**, 6
Chambers K. C., et al., 2016, *arXiv e-prints*, p. arXiv:1612.05560
Chawla C., Chatterjee S., Breivik K., Moorthy C. K., Andrews J. J., Sanderson R. E., 2022, *ApJ*, **931**, 107
Chubak C., Marcy G., Fischer D. A., Howard A. W., Isaacson H., Johnson J. A., Wright J. T., 2012, *arXiv e-prints*, p. arXiv:1207.6212
Clavel M., Dubus G., Casares J., Babusiaux C., 2021, *A&A*, **645**, A72
Conroy K. E., et al., 2020, *ApJS*, **250**, 34
Corral-Santana J. M., Casares J., Muñoz-Darias T., Bauer F. E., Martínez-Pais I. G., Russell D. M., 2016, *A&A*, **587**, A61
Czesla S., Schröter S., Schneider C. P., Huber K. F., Pfeifer F., Andreasen D. T., Zechmeister M., 2019, PyA: Python astronomy-related packages (ascl:1906.010)
Eaton J. A., Hall D. S., 1979, *ApJ*, **227**, 907
Eggleton P. P., 2012, *Journal of Astronomy and Space Sciences*, **29**, 145
El-Badry K., Burdge K. B., 2022, *Monthly Notices of the Royal Astronomical Society: Letters*, **511**, 24
El-Badry K., Quataert E., 2021, *Monthly Notices of the Royal Astronomical Society*, **502**, 3436
El-Badry K., Rix H.-W., 2022, *Monthly Notices of the Royal Astronomical Society*, **515**, 1266
El-Badry K., Burdge K. B., Mróz P., 2022a, *Monthly Notices of the Royal Astronomical Society*, **511**, 3089
El-Badry K., Seeburger R., Jayasinghe T., Rix H.-W., Almada S., Conroy C., Price-Whelan A. M., Burdge K., 2022b, *MNRAS*, **512**, 5620
El-Badry K., Conroy C., Fuller J., Kiman R., van Roestel J., Rodriguez A. C., Burdge K. B., 2022c, *Monthly Notices of the Royal Astronomical Society*, **517**, 4916
El-Badry K., et al., 2022d, *Monthly Notices of the Royal Astronomical Society*, **518**, 1057–1085
El-Badry K., et al., 2023, *Monthly Notices of the Royal Astronomical Society*, **521**, 4323
Eyer L., et al., 2022, Gaia Data Release 3. Summary of the variability processing and analysis, doi:10.48550/ARXIV.2206.06416, <https://arxiv.org/abs/2206.06416>
Foreman-Mackey D., Hogg D. W., Lang D., Goodman J., 2013, *Publications of the Astronomical Society of the Pacific*, **125**, 306
Fu J.-B., Gu W.-M., Zhang Z.-X., Yi T., Qi S.-Y., Zheng L.-L., Liu J., 2022, *The Astrophysical Journal*, **940**, 126
Gaia Collaboration et al., 2022, *arXiv e-prints*, p. arXiv:2206.05595
Gomel R., Faigler S., Mazeh T., 2020, *Monthly Notices of the Royal Astronomical Society*, **501**, 2822–2832
Gomel R., Faigler S., Mazeh T., 2021a, *Monthly Notices of the Royal Astronomical Society*, **504**, 2115–2121
Gomel R., Faigler S., Mazeh T., Pawlak M., 2021b, *MNRAS*, **504**, 5907
Gomel R., et al., 2022, *Astronomy & Astrophysics*
Gordon I., et al., 2022, *Journal of Quantitative Spectroscopy and Radiative Transfer*, **277**, 107949
Gray D. F., 1992, The observation and analysis of stellar photospheres.. Cambridge Astrophysics Vol. 20
Green G. M., Schlafly E., Zucker C., Speagle J. S., Finkbeiner D., 2019, *ApJ*, **887**, 93
Halbwachs J.-L., et al., 2022, Gaia Data Release 3. Astrometric binary star processing, doi:10.48550/ARXIV.2206.05726, <https://arxiv.org/abs/2206.05726>
Janssens S., et al., 2022, *A&A*, **658**, A129
Kobulnicky H. A., Molnar L. A., Cook E. M., Henderson L. E., 2022, *ApJS*, **262**, 12
Kollmeier J. A., et al., 2017, *arXiv e-prints*, p. arXiv:1711.03234
Lurie J. C., et al., 2017, *The Astronomical Journal*, **154**, 250
McClintock J. E., Remillard R. A., 2006, in , Vol. 39, Compact stellar X-ray sources. pp 157–213
Morris S. L., Naftilan S. A., 1993, *The Astrophysical Journal*, **419**, 344
Mowlavi N., et al., 2022, Gaia Data Release 3. The first Gaia catalogue of

- eclipsing binary candidates, [doi:10.48550/ARXIV.2211.00929](https://arxiv.org/abs/2211.00929), <https://arxiv.org/abs/2211.00929>
- O’Connell D. J. K., 1951, *Publications of the Riverview College Observatory*, **2**, 85
- Oke J. B., Gunn J. E., 1982, *Publications of the Astronomical Society of the Pacific*, **94**, 586
- Oke J. B., et al., 1995, *Publications of the Astronomical Society of the Pacific*, **107**, 375
- Pecaut M. J., Mamajek E. E., 2013, *ApJS*, **208**, 9
- Perley D. A., 2019, *PASP*, **131**, 084503
- Pešta M., Pejcha O., 2022, *arXiv e-prints*, p. [arXiv:2212.02553](https://arxiv.org/abs/2212.02553)
- Portegies Zwart S. F., Verbunt F., Ergma E., 1997, *A&A*, **321**, 207
- Pribulla T., Vaňko M., Chochol D., Hambálek L., Parimucha Š., 2011, *Astronomische Nachrichten*, **332**, 607
- Prochaska J., et al., 2020, *The Journal of Open Source Software*, **5**, 2308
- Prusti T., et al., 2016, *Astronomy & Astrophysics*, **595**
- Prša A., Zwitter T., 2005, *ApJ*, **628**, 426
- Rigault M., 2018, *ztfquery*, a python tool to access ZTF data, Zenodo, [doi:10.5281/zenodo.1345222](https://doi.org/10.5281/zenodo.1345222)
- Shahaf S., Bashi D., Mazeh T., Faigler S., Arenou F., El-Badry K., Rix H. W., 2023, *MNRAS*, **518**, 2991
- Sheinis A. I., Bolte M., Epps H. W., Kibrick R. I., Miller J. S., Radovan M. V., Bigelow B. C., Sutin B. M., 2002, *Publications of the Astronomical Society of the Pacific*, **114**, 851
- Vallenari A., Brown A., Prusti T., 2022, *Astronomy & Astrophysics*
- Warner B., 2003, *Cataclysmic Variable Stars*, [doi:10.1017/CBO9780511586491](https://doi.org/10.1017/CBO9780511586491).
- Wilson R. E., Devinney E. J., 1971, *ApJ*, **166**, 605
- Zahn J. P., 1977, *A&A*, **57**, 383

APPENDIX A: REJECTION OF CANDIDATES

In Table A1, we present a summary of our reasons for manually rejecting promising ellipsoidal variables (i.e. $\hat{q}_{\min} > 0.8$) that survived our initial automated vetting process ($\delta > -30^\circ$ and relative parallax / error > 3). The reasons are generally due to the variable being overluminous compared to the main sequence on the CMD, or visual inspection finding irregularities in the ZTF light curves.

APPENDIX B: TARGET SELECTION

In Table B1, we provide the coordinates, brightness, and modified minimum mass ratio of all target ellipsoidal variables in our vetted sample ($N = 14$).

APPENDIX C: LIGHT CURVES

We provide all of the ZTF g -band light curves for reference in Figure C1. We assume that the a light curve displaying ellipsoidal variability can be described using a sum of harmonics:

$$g = \bar{g} + \sum_{i=1}^2 a_i \cos\left(\frac{2\pi i(t - T_0)}{P}\right) \quad (\text{C1})$$

We use non-linear fitting techniques (i.e. Levenberg-Marquardt algorithm) to find the mean magnitude \bar{g} , best-fit coefficients a_i , and epoch of conjunction T_0 given the *Gaia* G -band period P , and overplot these fits in Figure C1. Candidates for which T_0 was later shifted by half a period based on radial velocity measurements are marked by an asterisk.

APPENDIX D: RADIAL VELOCITY PLOTS

We provide all of our radial velocity fits for ease of comparison in Figure D1. The mean radial velocities are subtracted so that all plots share the same vertical axis. As described in Section 4, color coding is by instrument used for each observation.

This paper has been typeset from a \LaTeX file prepared by the author.

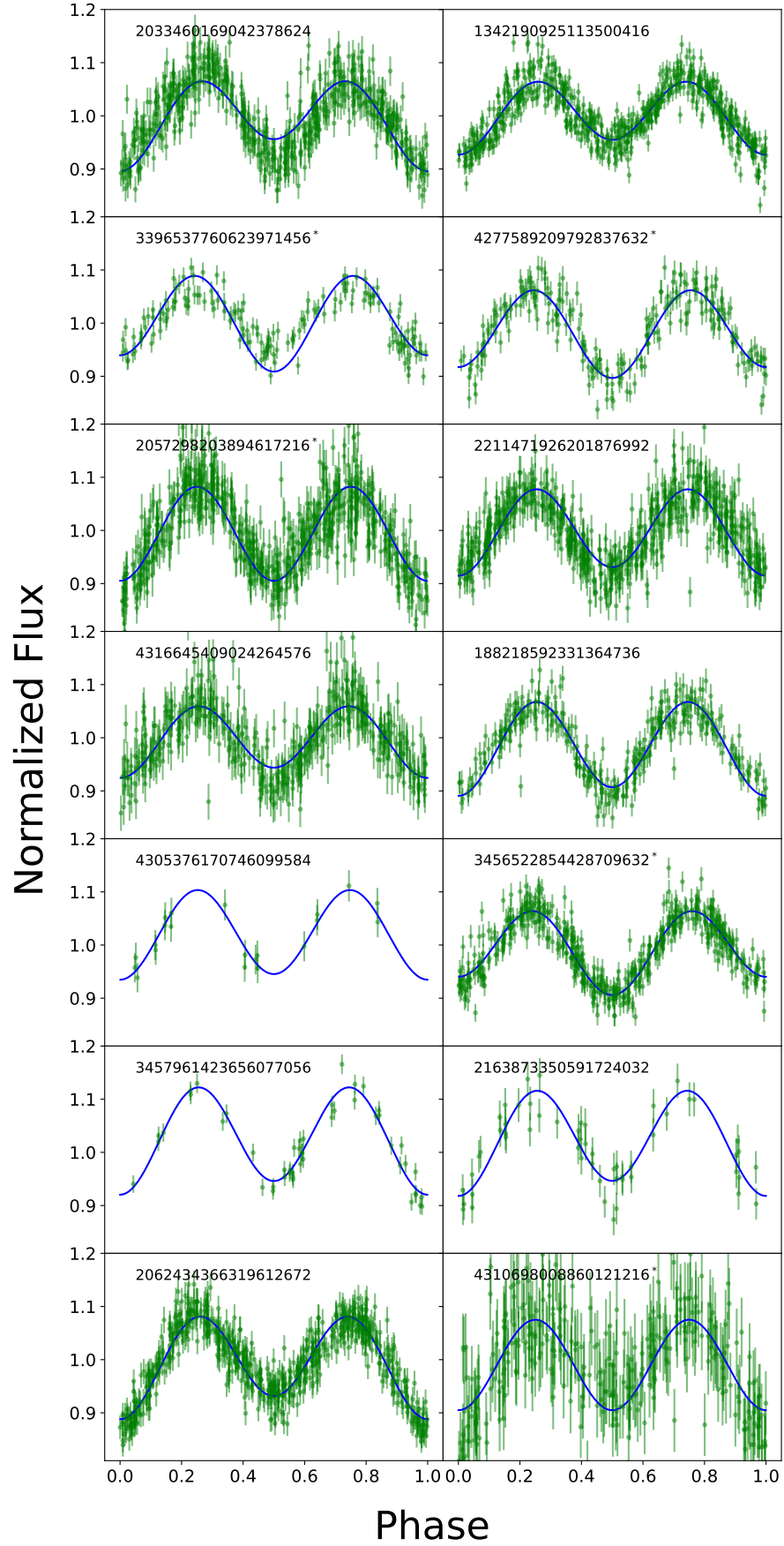


Figure C1. Comparison of g-band ZTF light curves for all observed ellipsoidal variables.

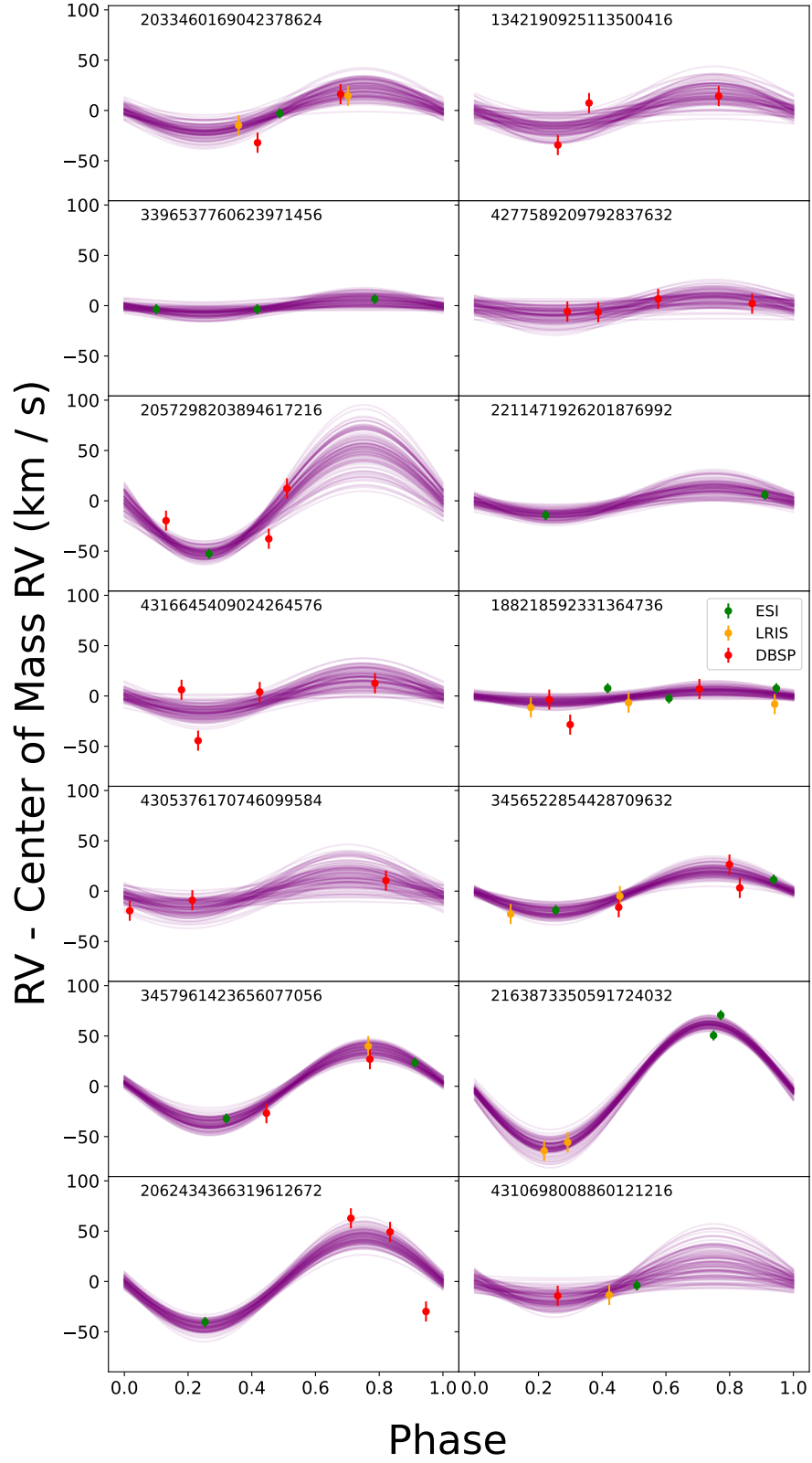


Figure D1. All radial velocity curves for observed ellipsoidal variables. Center of mass RVs are subtracted for ease of comparison.

Table A1. Summary of reasons for rejection of promising candidates ($\hat{q}_{\min} > 0.8$) in vetted sample (apparent G -band magnitude < 17 , `parallax_over_error` > 3 , and well-constrained extinctions from the 3D dust map of [Green et al. \(2019\)](#)).

Gaia Source ID	Reason for Rejection
1842474999287779456	Above main sequence on CMD
246694542008676224	Large difference between light curve minima
6858874244124457728	Not enough ZTF data
4115129387457079808	Above main sequence on CMD
4090783421259714048	Sharp variation in r -band ZTF light curve
4056769479221855872	Not enough ZTF data
2180310877623317632	Above main sequence on CMD
4513065361686161408	Poorly sampled ZTF light curves
4069146883471008384	Above main sequence on CMD
4245202918693685888	Not enough ZTF data
2118894735067533568	Above main sequence on CMD
4294656413422555136	Evolved onto giant branch
3415519106594116864	Large difference between light curve minima
4268159896853550720	Not enough ZTF data
2019379999263502080	Above main sequence on CMD
4308281733324882688	Noisy r -band ZTF light curve
4316223093502225920	Noisy ZTF light curves
4308186591192260224	Above main sequence on CMD
4062968796360712192	Not enough ZTF data
6033056688573451904	Noisy g -band ZTF light curve
4063595075664390656	Noisy ZTF light curves
4044200716984124800	Not enough ZTF data
4602733180577371136	Above main sequence on CMD
4505025384714693632	Noisy ZTF light curves
2065168057153338752	Atypical r -band ZTF light curve
4320737104132599040	Above main sequence on CMD
237183422828574208	Large difference between light curve minima
187446224071740544	Above main sequence on CMD
4302060043674728320	Above main sequence on CMD
3309994169609595264	Above main sequence on CMD
439282146866334848	Above main sequence on CMD
4096747756468453888	Above main sequence on CMD
4067422028923930880	Evolved onto giant branch
3019860195232390528	Noisy ZTF light curves
3389233807958342912	Poorly sampled ZTF light curves
4310887438426691840	Significant difference between light curve maxima
448105693321340800	Above main sequence on CMD
4107013003158530048	Above main sequence on CMD
504992569522209792	Above main sequence on CMD
3427530553869533440	Atypical r -band ZTF light curve
2179940956377621888	Not enough ZTF data
4117615245815921024	Noisy g -band ZTF light curve
4323490762226799232	Not enough ZTF data
4151452613074058880	Not enough ZTF data
4124801898687751040	Above main sequence on CMD
4068633617699998080	Not enough ZTF data
1731244348571923200	Above main sequence on CMD
4067808571662706688	Not enough ZTF data
4143833001843654912	Above main sequence on CMD
4070409432055253760	Not enough ZTF data
4056017172771375616	Not enough ZTF data
6038453229081523072	Not enough ZTF data

Table B1. Final target list of ellipsoidal binaries with potential compact object companions.

<i>Gaia</i> Source ID	RA (hms)	Dec (dms)	Apparent G Magnitude	Period	\hat{q}_{\min}	Peak-to-Peak Amplitude
2033460169042378624	19 51 11.59	+30 40 22.10	16.97	0.270854 ± 0.000057	0.91 ± 0.22	0.169
1342190925113500416	17 38 36.73	+36 49 21.43	16.82	0.279545 ± 0.000078	0.52 ± 0.12	0.137
3396537760623971456	05 46 08.40	+17 15 39.10	16.49	0.311336 ± 0.000074	0.69 ± 0.17	0.180
4277589209792837632	18 14 39.86	+02 06 01.49	16.12	0.329189 ± 0.000082	1.18 ± 0.34	0.165
2057298203894617216	20 22 57.10	+36 16 52.38	16.76	0.352784 ± 0.000096	1.01 ± 0.26	0.177
2211471926201876992	22 54 54.66	+65 02 53.18	16.81	0.353515 ± 0.000108	0.82 ± 0.20	0.163
4316645409024264576	19 29 23.02	+13 53 40.43	16.99	0.390803 ± 0.000094	1.01 ± 0.25	0.135
188218592331364736	05 14 08.92	+38 49 16.56	16.58	0.395750 ± 0.000142	1.08 ± 0.27	0.177
4305376170746099584	19 50 46.50	+13 42 34.64	16.97	0.409171 ± 0.000104	1.07 ± 0.29	0.169
3456522854428709632	06 00 35.88	+35 58 00.84	16.68	0.430926 ± 0.000134	1.04 ± 0.27	0.158
3457961423656077056	05 52 35.93	+38 31 13.35	16.48	0.458269 ± 0.000152	1.14 ± 0.28	0.202
2163873350591724032	20 59 40.91	+47 16 10.99	16.97	0.481034 ± 0.000174	1.04 ± 0.26	0.198
2062434366319612672	20 13 10.48	+40 24 56.28	16.36	0.721862 ± 0.000404	1.06 ± 0.26	0.193
4310698008860121216	19 06 17.45	+09 34 08.08	16.99	0.751384 ± 0.000436	1.62 ± 0.46	0.170